

Do Pathology Foundation Models Encode Disease Progression? A Pseudotime Analysis of Visual Representations

Pritika Vig^{1,2} Ren-Chin Wu³ William Lotter^{2,4,5}

Abstract

Vision foundation models trained on discretely sampled images achieve strong performance on classification benchmarks, yet whether their representations encode the continuous processes underlying their training data remains unclear. This question is especially pertinent in computational pathology, where we posit that models whose latent representations implicitly capture continuous disease progression may better reflect underlying biology, support more robust generalization, and enable quantitative analyses of features associated with disease transitions. Using diffusion pseudotime, a method developed to infer developmental trajectories from single-cell transcriptomics, we probe whether foundation models organize disease states along coherent progression directions in representation space. Across four cancer progressions and six models, we find that all pathology-specific models recover trajectory orderings significantly exceeding null baselines, with vision-only models achieving the highest fidelities ($\tau > 0.78$ on CRC-Serrated). Model rankings by trajectory fidelity on reference diseases strongly predict few-shot classification performance on held-out diseases ($\rho = 0.92$), and exploratory analysis shows cell-type composition varies smoothly along inferred trajectories in patterns consistent with known stromal remodeling. Together, these results demonstrate that vision foundation models can implicitly learn to represent continuous processes from independent static observations, and that trajectory fidelity provides a complementary measure of representation quality beyond downstream performance. While demonstrated in pathology, this framework could

be applied to other domains where continuous processes are observed through static snapshots.

1. Introduction

Vision foundation models for computational pathology (CPath) now achieve state-of-the-art performance across diverse diagnostic tasks, from tumor classification to mutation prediction (Chen et al., 2024; Zimmermann et al., 2024; Xu et al., 2024; Lu et al., 2024; Xiang et al., 2025). These models process hematoxylin and eosin (H&E) stained whole slide images (WSIs) by dividing them into smaller image patches and generating embeddings for each patch. The performance of these embeddings is primarily assessed using discrete classification benchmarks (Kang et al., 2023; Campanella et al., 2025; Bareja et al., 2025).

However, relying exclusively on downstream performance benchmarks provides insufficient understanding of both the ability to generalize in clinical settings and the extent to which foundation model representations encode underlying disease biology. Methods targeting the latter especially have the potential to advance our understanding of connections between histological features and patient outcomes. The importance of understanding foundation model representations is underscored by recent findings highlighting their fragility under distribution shifts and stain variations (Tizhoosh, 2025; de Jong et al., 2025; Kömen et al., 2024).

Robust pathology foundation models will require representations that capture true biological structure. One natural test of this quality is disease progression: while downstream benchmarks typically assess discrete classification, disease itself progresses continuously. Understanding what these transition states look like morphologically is particularly important in oncology, where predicting which lesions will progress has direct clinical stakes. More broadly, the question of whether vision models implicitly learn continuous processes from discretely sampled images extends to many other biomedical and natural image domains.

Given its importance, methods have been developed to infer temporal ordering from independent biological samples in other applications. Among these, diffusion pseudotime

¹Massachusetts Institute of Technology, Cambridge, MA, USA ²Department of Data Science, Dana-Farber Cancer Institute, Boston, MA, USA ³Department of Pathology, Dana-Farber Cancer Institute, Boston, MA, USA ⁴Brigham and Women's Hospital, Boston, MA, USA ⁵Harvard Medical School, Boston, MA, USA. Correspondence to: Pritika Vig <pritikav@mit.edu>.

(DPT; Haghverdi et al. 2016) reconstructs developmental trajectories from single-cell transcriptomics, where input features are gene expression measurements with direct biological meaning. DPT constructs a nearest-neighbor graph over samples and computes transition probabilities via random walks, yielding a pseudotime coordinate that orders cells along a continuous process.

In this paper, we apply this logic to the opaque learned representations of foundation models, with the intuition that if DPT recovers correct disease progression ordering from these embeddings, it provides evidence that the representation implicitly encodes progression-relevant structure. We operationalize this as an ordering problem: for each disease cohort, we embed histopathology patches using a foundation model, compute diffusion pseudotime, and quantify trajectory fidelity between inferred pseudotime and ordinal ground-truth class labels. We perform this procedure for six models and four disease progressions, and subsequently assess associations with downstream performance generalization and biological features.

Our contributions are as follows:

- We demonstrate that pathology foundation models implicitly encode disease progression as low-dimensional manifolds, recovering temporal ordering from static snapshots without supervision.
- We find trajectory fidelity correlates with few-shot generalization performance: models preserving progression structure on reference cohorts achieve higher classification task accuracy on held-out diseases (mean $\rho = 0.92$), offering a proxy for generalization.
- We show initial evidence that learned representations encode biological processes at sub-class granularity: cell-type composition varies smoothly along the inferred disease manifold in patterns consistent with known stromal remodeling, providing opportunities to understand biological changes more finely than discrete progression state labels.

2. Related Work

2.1. Representation Learning in Vision Models

Feature learning in convolutional neural networks (CNNs) has been extensively characterized through visualization and diagnostic analyses (Zeiler & Fergus, 2014); in contrast, understanding how vision transformers (ViTs) organize learned representations remains comparatively underdeveloped. Since all state-of-the-art pathology models evaluated in this work are ViT-based, this emerging literature is directly relevant to our analysis.

Unlike CNNs, which enforce hierarchical feature abstrac-

tion through localized receptive fields and pooling, Raghu et al. (2022) show that Vision Transformers exhibit highly uniform representation similarity across layers, with substantial overlap between early and late representations. This uniformity arises from early global information mixing via self-attention and strong residual connections that propagate features throughout the network. Importantly, representational uniformity at the layer level does not imply semantic uniformity at the neuron level: while entire layers remain highly similar in representation space, the distribution of concepts encoded by individual neurons shifts with depth. Dorszewski et al. (2025) demonstrate that ViTs exhibit a gradual progression in neuron-level concept complexity, from colors and textures in early layers to object- and class-level semantics in later layers.

2.2. Trajectory Modeling

Disease progression is a continuous dynamic process, but CPath datasets largely consist of static snapshots of disjoint tissue samples captured at single timepoints. This mirrors a fundamental challenge in single-cell trajectory inference which Diffusion Pseudotime (DPT; Haghverdi et al., 2016) was developed to address. DPT defines a progression ordering between data samples through a Markov diffusion process with transition probabilities that are based on pairwise feature similarities. By aggregating transition probabilities over random walks of all lengths, DPT induces a multiscale diffusion distance that approximates geodesic structure on the data manifold. Empirically, these diffusion-based orderings yield stable progression orderings that are more robust to local sampling density variation than distance-based approaches (i.e, Euclidean distance in the original feature space).

2.3. Pathology Foundation Models and Benchmarking

Numerous CPath foundation models have recently been developed, which are trained in a self-supervised fashion using large-scale datasets of H&E-stained slides. These models commonly operate at a patch-level to generate embeddings from cropped H&E patches and are typically evaluated using downstream task benchmarks using discrete clinical prediction problems, often via linear probing on frozen embeddings (Kang et al., 2023; Campanella et al., 2025; Bareja et al., 2025). While these benchmarks provide broad coverage across tasks and cohorts, they assess discriminative performance between labeled states rather than whether learned representations preserve the continuous biological processes linking those states.

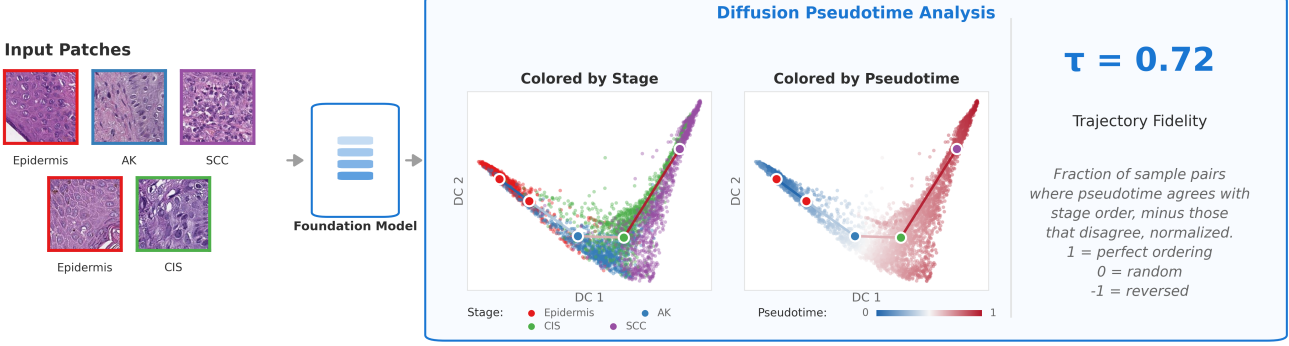


Figure 1. Overview of trajectory fidelity evaluation. H&E patches representing disease states (here: skin squamous cell carcinoma progression from epidermis through actinic keratosis and carcinoma in situ to invasive SCC) are embedded by a foundation model. We apply diffusion pseudotime analysis to the embedding space, visualized here via diffusion components (DC1, DC2). Left: patches colored by ground-truth class show spatial organization reflecting disease progression. Right: the same embedding colored by inferred pseudotime reveals a continuous gradient. Trajectory fidelity (τ) quantifies agreement between pseudotime ordering and ground-truth ordinal class labels using Kendall's rank correlation; $\tau = 0.72$ indicates strong preservation of biological progression structure.

3. Methods

3.1. Diffusion Pseudotime

Given a set of d -dimensional feature vectors $\mathbf{X} = \{\mathbf{x}_1, \dots, \mathbf{x}_n\}$ representing biological samples, diffusion pseudotime (DPT) identifies a relative ordering along an underlying continuous process by computing transition probabilities between nearby points in feature space. Starting from a designated root sample \mathbf{x}_{root} , DPT aggregates these probabilities across random walks of all lengths, ultimately outputting a pseudotime coordinate $t_i = \text{dpt}(\mathbf{x}_{\text{root}}, \mathbf{x}_i) \in \mathbb{R}$ for each sample i that quantifies its progression distance from the root. In the original single-cell genomics work, DPT successfully ordered 3,934 hematopoietic cells (42-dimensional gene expression features) from early precursors through intermediate states to mature blood cells and identified the branching point between erythroid and endothelial lineages, recovering the known developmental timeline (Haghverdi et al., 2016).

We apply this approach to foundation model embeddings $\mathbf{X} = \{\mathbf{x}_1, \dots, \mathbf{x}_n\}$ representing histopathology patches across disease states. We build a transition matrix \mathbf{T} by constructing a weighted k -nearest-neighbor graph ($k = 100$) over patch embeddings using cosine distance. To account for varying sampling densities on the manifold, we employ a locally scaled Gaussian kernel (Haghverdi et al., 2016). The transition probability between patches \mathbf{x}_i and \mathbf{x}_j is:

$$T_{ij} = \frac{K(\mathbf{x}_i, \mathbf{x}_j)}{Z_i} \quad (1)$$

$$K(\mathbf{x}_i, \mathbf{x}_j) = \exp\left(-\frac{\|\mathbf{x}_i - \mathbf{x}_j\|_{\text{cosine}}^2}{2\sigma_i\sigma_j}\right)$$

where σ_i is the local kernel width determined by the distance to the k -th nearest neighbor of \mathbf{x}_i , and $Z_i = \sum_{j \in \mathcal{N}_k(i)} K(\mathbf{x}_i, \mathbf{x}_j)$ is the row-normalizing constant ensuring $\sum_j T_{ij} = 1$.

For two patches indexed by i and j , the DPT distance is the Euclidean distance between their accumulated transition probabilities, $\text{dpt}(i, j) = \|\mathbf{M}(i, \cdot) - \mathbf{M}(j, \cdot)\|_2$. \mathbf{M} is the accumulated transition matrix summing over random walks of all lengths:

$$\mathbf{M} = \sum_{t=1}^{\infty} \tilde{\mathbf{T}}^t = (\mathbf{I} - \tilde{\mathbf{T}})^{-1} - \mathbf{I} \quad (2)$$

Here $\tilde{\mathbf{T}} = \mathbf{T} - \psi_0\psi_0^T$ is the transition matrix with the stationary eigenspace (corresponding to eigenvalue $\lambda_0 = 1$) removed. In practice, we approximate \mathbf{M} via spectral decomposition:

$$\mathbf{M} \approx \sum_{i=1}^{n_{\text{dc}}} \frac{1}{1 - \lambda_i} \psi_i \psi_i^T \quad (3)$$

where $\{\lambda_i, \psi_i\}$ are the eigenvalue-eigenvector pairs of $\tilde{\mathbf{T}}$, ordered by decreasing eigenvalue magnitude.

Fixing a known root patch r (the medoid of the earliest disease class), the pseudotime coordinate of patch i is $t_i = \text{dpt}(r, i)$. We compute DPT using the Scanpy (Wolf et al., 2018) library. Hyperparameter selection is detailed in Appendix A.

3.2. Trajectory Fidelity Metric

To evaluate the agreement between the inferred diffusion pseudotime (continuous) and ground-truth disease classes (ordinal states), we computed Kendall's Rank Correlation Coefficient (τ) (Haghverdi et al., 2016; Kendall, 1938). We employed the τ_b variant (via `scipy.stats`) to explicitly account for the substantial ties inherent to discrete staging labels. A value of $\tau = 1$ indicates that the inferred pseudotime

strictly preserves the biological order of disease progression, where a value of 0 indicates random concordance.

3.3. Disease Progression Cohorts

We analyzed four biologically validated cancer progressions using expert-annotated 224×224 pixel patches from the SPIDER dataset (Nechaev et al., 2025b), which provides H&E-stained patches at $20\times$ magnification from the HISTAI collection (Nechaev et al., 2025a). Institutional sources and slide mappings of the four scanners used are not publicly disclosed, precluding explicit batch effect analysis. SPIDER was not included in training data for any foundation models we evaluate. Using the patch-level class labels, we defined four discrete progression trajectories based on established pathological models:

Skin Squamous Cell Carcinoma (SCC). *Epidermis* \rightarrow *Actinic keratosis* \rightarrow *SCC in situ* \rightarrow *Invasive SCC*. This trajectory models classic UV-induced progression from precursor lesions to invasive malignancy (Ratushny et al., 2012).

Colorectal Conventional Pathway. *Adenoma (low grade)* \rightarrow *Adenoma (high grade)* \rightarrow *Adenocarcinoma (low grade)* \rightarrow *Adenocarcinoma (high grade)*. This follows the canonical adenoma-carcinoma sequence, representing gradual accumulation of genetic alterations from benign neoplasia to undifferentiated carcinoma (Fearon & Vogelstein, 1990).

Colorectal Serrated Pathway. *Hyperplastic polyp* \rightarrow *Sessile serrated lesion (SSL)* \rightarrow *Adenocarcinoma (high grade)*. This captures the alternative serrated pathway, distinct from the conventional sequence (De Palma et al., 2019). We note that SSL and high-grade adenocarcinoma span a relatively large morphological gap for which intermediate stages can be assigned (e.g., SSL with Dysplasia), but these more granular labels are not provided in the dataset.

Breast Ductal Carcinoma (BDC). *DCIS (low-grade)* \rightarrow *DCIS (high-grade)* \rightarrow *Invasive carcinoma*. While direct temporal evolution from low- to high-grade DCIS is one plausible trajectory, these grades can also arise via independent evolutionary pathways (Hulahan & Angel, 2024), and thus, at a minimum, this sequence reflects a progression of histological severity.

We standardized each disease progression to 1,000 patches per class using slide-aware sampling, which caps a single slide’s contribution at 50 patches to mitigate intra-sample correlation and slide-level batch effects. This resulted in 4,000 patches for four-class cohorts (cSCC, colorectal conventional) and 3,000 for colorectal serrated. Due to scarcity in the BDC dataset, the high-grade DCIS class was constrained to 714 patches from 39 available slides, yielding a total cohort of 2,714. Manifold robustness analysis confirmed that trajectory structure remains invariant to these minor class density fluctuations (see Appendix B and D).

3.4. Foundation Models

We evaluated six foundation models spanning distinct pre-training paradigms, including one natural image baseline, DINOv2 (Oquab et al., 2024) (ViT-L/14, $d = 1024$), and five pathology-specific models. These comprise two methodological families: vision-only models trained with self-supervised learning, and vision-language models trained with text supervision. The vision-only pathology models—UNI-2 (Chen et al., 2024) (ViT-H/14, $d = 1536$), Virchow-2 (Zimmermann et al., 2024) (ViT-H/14, $d = 1280$), and Prov-GigaPath (Xu et al., 2024) (ViT-g/14, $d = 1536$)—all adapt DINOv2 self-distillation to histopathology. Broadly, these models differ in their scaling strategies and pathology-specific optimizations: UNI-2 focuses on architectural width (Custom ViT-H), Prov-GigaPath emphasizes massive real-world data scale (1.3B tiles from 171k slides), and Virchow-2 integrates multi-resolution training (5x-40x) with a domain-adapted DINOv2 objective. For vision-language models, CONCH (Lu et al., 2024) (ViT-B/16, $d = 512$) uses a CoCa-style objective and MUSK (Xiang et al., 2025) (ViT-L/16, $d = 1024$) uses a BEiT-3 multimodal architecture. For all models, we extract [CLS] token embeddings from the patch encoder. For vision-language models, we use embeddings from the vision encoder prior to text-alignment projection to isolate visual representations.

3.5. Intrinsic Dimension Estimation

To characterize the emergence of progression structure across network depth (Section 4.2), we estimate the intrinsic dimension (ID) of embeddings at intermediate layers. ID quantifies the minimum number of variables needed to describe the representation’s structure; a low ID relative to the raw embedding dimension indicates compression onto a lower-dimensional manifold. We use the TWO-NN estimator (Facco et al., 2017) applied to 2,000 subsampled patches.

4. Results

4.1. Foundation Models Encode Biological Progression Trajectories

4.1.1. TRAJECTORY FIDELITY ACROSS MODELS

We evaluated trajectory fidelity across five computational pathology foundation models spanning two pre-training paradigms: vision-language (CONCH, MuSK), and vision-only (UNI-2, Virchow-2, Prov-GigaPath). We additionally compare to natural image foundation model baselines (DINOv2). Figure 2 reports Kendall’s τ between inferred diffusion pseudotime and ground-truth disease state for final-layer embeddings across all four progression cohorts.

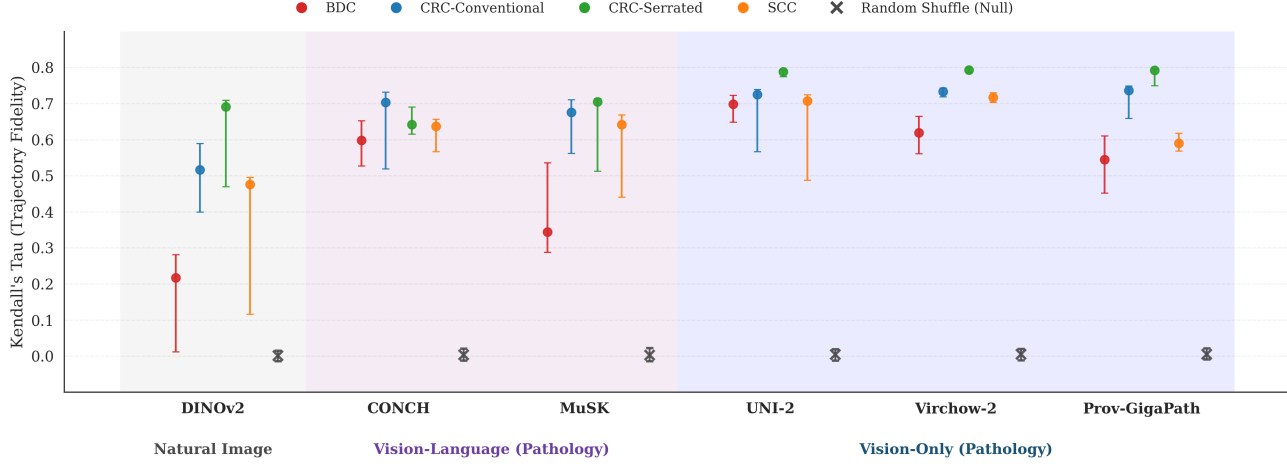


Figure 2. Trajectory fidelity across foundation models and disease progressions. Kendall's τ between diffusion pseudotime and ground-truth class labels for six foundation models across four cancer progressions. All models significantly exceed the null baseline (gray \times , label-shuffled controls). Vision-only pathology models (UNI-2, Virchow-2, Prov-GigaPath) achieve the highest and most consistent fidelity, while the natural image baseline (DINOv2) shows weaker and more variable recovery. Exact values reported in Appendix C.

All CPath models achieved trajectory fidelity significantly exceeding the label-shuffled null baseline, with 95% CIs showing clear separation from the null distribution centered near zero. This null control randomizes the assignment of ordinal progression state labels to patches while preserving the embedding geometry and inferred pseudotime values. The separation from null confirms that patches with similar pseudotime values share disease states beyond what would be expected by chance, indicating that the embedding geometry places biologically adjacent states nearby. The natural image baseline (DINOv2) achieved moderate fidelity on colorectal progressions but failed to recover BDC progression ($\tau = 0.22$), approaching null performance. This suggests that general visual features capture some progression-relevant structure, but domain-specific training is necessary for consistent recovery across tissue types.

Vision-only CPath models (UNI-2, Virchow-2, Prov-GigaPath) demonstrated the strongest and most consistent fidelity across progressions, with CRC-Serrated yielding the highest scores ($\tau > 0.78$). The vision-language models showed greater variability: CONCH performed comparably to vision-only models on colorectal progressions but showed reduced fidelity on BDC, while MuSK exhibited the largest variance ($\tau = 0.71$ on CRC-Serrated vs. $\tau = 0.35$ on BDC). Notably, models with higher trajectory fidelity also exhibited tighter confidence intervals across bootstrap samples.

4.1.2. PERMUTATION TEST VALIDATION

Do foundation model representations simply capture discrete disease labels, or are they actually encoding a continuum between disease states? If embeddings simply cluster

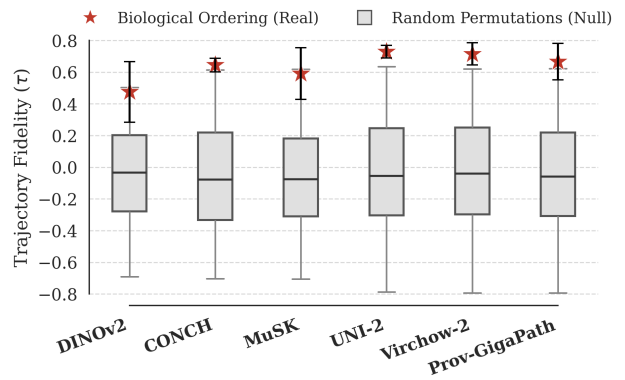


Figure 3. Trajectory fidelity reflects biological ordering, not class structure. Stars: mean τ for true progression order across four cohorts (95% CI). Boxplots: null distributions from permuted class label orderings, pooled across cohorts. All models exceed the null median; vision-only CPath models show clearest separation.

by diagnosis, any ordering of well-separated classes could yield high τ . To test this, we computed trajectory fidelity for every possible ordinal sequence of the class labels, while keeping the embeddings, pseudotime values, and class assignments fixed.

We first examine results aggregated across all four disease progressions. For each model, we averaged the τ values from the true biological orderings across progressions and compared this to the distribution of τ values from all permuted orderings pooled across progressions. If discrete clustering alone drove our results, the trajectory fidelity for the true biological ordering would be indistinguishable from those of the permuted orderings. Instead, the null distributions center around zero and for all CPath models, the true

ordering mean τ falls outside or at the upper boundary of the null distributions (Figure 3), with vision-only models showing the clearest separation. This indicates that the embeddings do not merely separate disease states but arrange them in a geometry that specifically reflects the biological progression direction. Per-progression results confirm this pattern holds for individual pathologies (Appendix E), though with more variability, particularly for DINOv2 and MuSK on BDC.

4.2. Emergence of Continuous Structure Across Network Depth

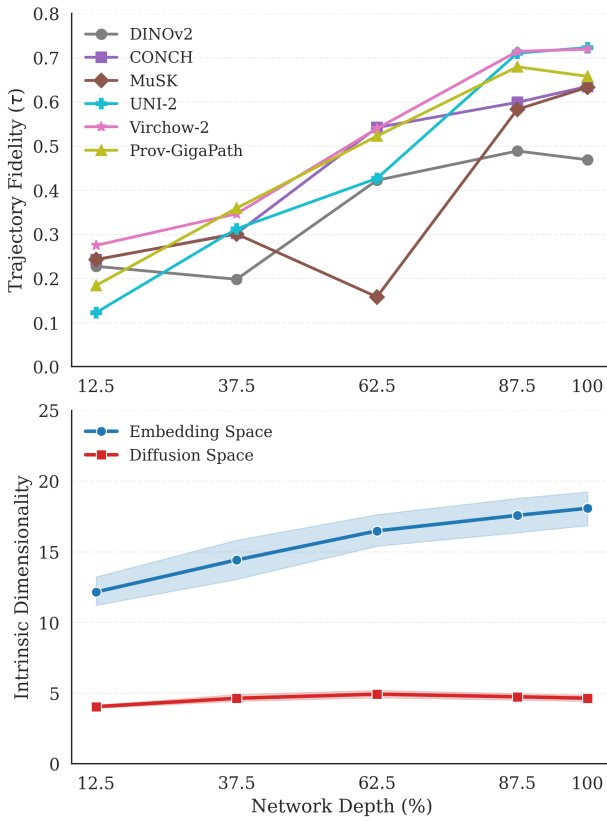


Figure 4. Trajectory fidelity emerges progressively across network depth. Top: Trajectory fidelity (τ) using [CLS] token embeddings, averaged across progressions. Vision-only pathology models (UNI-2, Virchow-2, Prov-GigaPath) and CONCH show steady improvement through 87.5–100% depth, while MuSK exhibits a mid-network dip before recovery. Bottom: Average intrinsic dimensionality of raw embeddings (blue) expands across layers (~ 12 to ~ 18) while diffusion manifold dimensionality (red) remains stable (≈ 4 –5). Shaded regions show 95% CI across models and progressions.

When does the observed progression structure emerge in foundation model representations? To investigate this, we extracted [CLS] embeddings from intermediate transformer blocks at five relative depths (12.5%, 37.5%, 62.5%, 87.5%, and 100%) across all models and progressions. As shown in

Figure 4 (Top), average trajectory fidelity increases across network depth for all models, though the rate and pattern of emergence varies by architecture.

Early layers encode some progression-relevant structure: at 12.5% depth, trajectory fidelity ranges from $\tau \approx 0.1$ to $\tau \approx 0.3$ across models (Figure 4, Top). This structure is substantially refined through the network, with final values spreading to $\tau \approx 0.45$ –0.70. The vision-only CPath models (Virchow-2, UNI-2, Prov-GigaPath) and CONCH show the strongest and most consistent improvement, with steady gains that steepen in later layers. MuSK shows non-monotonic behavior, with trajectory fidelity declining from $\tau \approx 0.30$ at 37.5% to $\tau \approx 0.16$ at 62.5% before recovering to $\tau \approx 0.64$ at 100%. This pattern may reflect its BEiT-3 architecture, which activates vision-language fusion experts only in later layers (Wang et al., 2022). At early layers, DINOv2 is consistent with the CPath models but ends with the lowest trajectory fidelity ($\tau < 0.5$ throughout), suggesting that while natural image pretraining can detect lower-level progression-relevant signals, domain-specific pretraining becomes increasingly important for refining this structure.

The refinement of trajectory fidelity coincides with expanding representational complexity (Figure 4, Bottom). Raw embedding intrinsic dimensionality increases from ~ 12 to ~ 18 dimensions across layers, tracking trajectory fidelity improvement. Yet diffusion manifold dimensionality remains stable at ≈ 4 –5 dimensions throughout, suggesting that deeper layers build richer representational capacity while the underlying biological progression signal remains intrinsically low-dimensional. Analysis using patch token embeddings is also contained in Appendix F.

4.3. Trajectory Fidelity Tracks Few-Shot Generalization

We next asked whether trajectory fidelity correlates with downstream classification performance. These are geometrically distinct properties: trajectory fidelity measures preservation of biological ordering, while few-shot classification measures discriminative margins between class centroids. A correlation would suggest that encoding progression structure confers broader representational benefits.

We first examined the relationship between trajectory fidelity and classification performance within individual disease progressions (Appendix Figure 13). For each progression, we computed the correlation between τ and 5-shot F1 score on label classification with a multi-class logistic regression model (see Appendix G.1 for methodological details). We find that these correlations are consistently strong: $\rho = 0.94$ (BDC), $\rho = 0.83$ (SCC), $\rho = 0.77$ (CRC-Conv), and $\rho = 0.77$ (CRC-Serr), with a mean of $\rho = 0.83$. This indicates that, controlling for disease-specific baseline difficulty, models that better preserve progression geometry achieve substantially higher few-shot classification perfor-

mance.

To test whether this relationship transfers across disease types, we employed a leave-one-out protocol. This provides a stringent test of generalization: if trajectory fidelity on unrelated diseases predicts few-shot performance on a held-out tissue type, it suggests that τ captures fundamental aspects of representation quality rather than solely disease-specific structure. For each of the four progressions, we computed the mean trajectory fidelity across the three reference cohorts (excluding the target) and evaluated 5-shot classification F1 on the held-out progression. We then assessed whether model rankings by reference τ predict rankings by held-out F1 (Figure 5). We find that reference manifold quality strongly predicts held-out classification performance: Spearman rank correlations are $\rho = 1.00$ (CRC-Conv), $\rho = 0.94$ (BDC), $\rho = 0.89$ (SCC), and $\rho = 0.83$ (CRC-Serr), with a mean of $\rho = 0.92$. This indicates that model rankings by trajectory fidelity on reference diseases reliably transfer to held-out tissue types, even when the target disease was excluded from the ranking criterion.

4.4. Trajectory Exploration

Now that we have established that CPath models capture disease trajectories via pseudotime, we explore what additional insights this affords. A critical question in histopathology is how cellular composition changes throughout progression, potentially reflecting phenomena such as immune evasion. Pseudotime enables analysis of transitional disease states, offering a more granular ordering of patches than discrete labels. To validate the biological relevance of this ordering, we analyzed the cellular composition of the colorectal conventional trajectory using the Histoplus cell segmentation and classification model (Adadj et al., 2025). Histoplus was trained on colon adenocarcinoma, specifically the TCGA-COAD dataset, and has demonstrated strong generalization to external cohorts. We quantified cell type abundance on $N = 8,000$ patches evenly sampled from each class along pseudotime in the UNI-2 embedding space and visualized the standardized dynamics in Figure 6.

Consistency with the adenoma–carcinoma continuum. The inferred trajectory places high-grade adenoma and low-grade adenocarcinoma patches in close proximity in pseudotime, with overlap. This distribution matches prior pathology consensus that these classes can be difficult to separate visually when invasion is not captured in the local field of view (Schlemper et al., 2000).

Pseudotime captures a biologically plausible non-monotonic stromal trajectory. We observe a V-shaped pattern in fibroblast abundance centered near the adenoma–adenocarcinoma transition region. Fibroblast abundance appears to decrease across the pseudotime region representing Adenoma high grade, consistent with epithelial over-

growth and back-to-back glandular architecture that compresses the stromal compartment, reducing the space occupied by fibroblasts during dysplasia (Fleming et al., 2012). Subsequently, fibroblast abundance shows an increase over pseudotime for Adenocarcinoma Low Grade, potentially reflecting the onset of the desmoplastic reaction and activation of cancer-associated fibroblasts that accompany early invasive growth in colorectal carcinoma (Ueno et al., 2021; Kalluri, 2016). This trend emerges smoothly over pseudotime despite substantial overlap in discrete class labels, suggesting that the inferred ordering captures meaningful structure that is obscured by coarse categorical annotations. See Appendix H for robustness analyses.

Progressive ordering within advanced disease. Although cancer cell abundance increases early along pseudotime and plateaus by mid trajectory ($t \simeq 0.4$), neutrophilic infiltration continues to increase through the ordered Adenocarcinoma high grade samples. This suggests the inferred trajectory organizes meaningful within-class variation, consistent with the prognostic significance of intratumoral neutrophil density in colorectal cancer (Shaul & Fridlender, 2019).

5. Discussion

Across all evaluated CPath foundation models, disease progression emerges as a low-dimensional ordered structure in their representation spaces. All evaluated CPath models recovered trajectory orderings significantly exceeding null baselines, demonstrating that self-supervised learned embeddings organize disease states along coherent progression directions. However, fidelity varied meaningfully across models and disease types: vision-only models achieved the highest and most consistent performance, while vision-language models, especially MuSK, showed greater variability across cohorts.

Trajectory fidelity emerges progressively across network depth. For [CLS] token embeddings, trajectory fidelity increases steadily throughout the network, with vision-only pathology models showing the strongest gains between 37.5–87.5% of relative depth. This monotonic improvement contrasts with patch token embeddings, which show a saturating pattern with rapid gains between 30–60% depth followed by plateau. The trajectory learning pattern observed in the patch mean tokens aligns well with literature showing that mid-network ViT layers encode texture- and morphology-level concepts before later abstraction (Dorszewski et al., 2025).

Trajectory fidelity complements classification benchmarks by offering insights into continuous progressions rather than discrete labels and classification performance. Classification performance reflects how well a representation supports separation between labeled classes, not

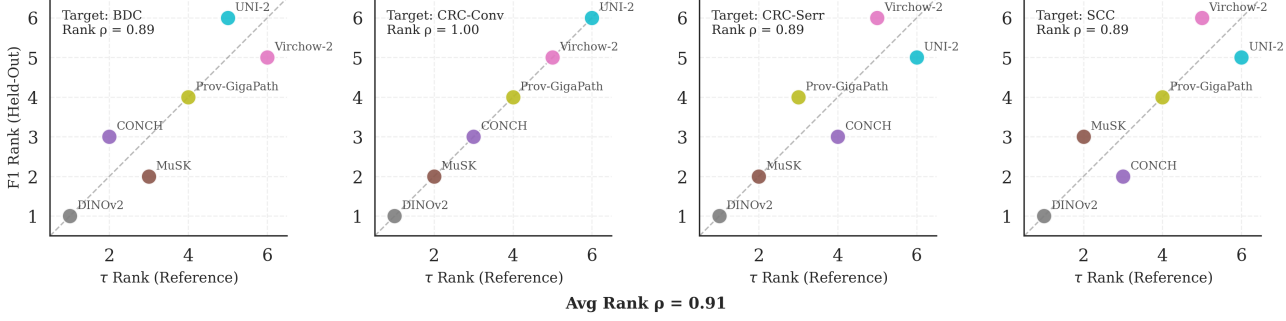


Figure 5. Model rankings by trajectory fidelity transfer to held-out diseases. Cross-task generalization using a leave-one-out protocol. For each target disease (panel), we ranked models by mean τ on the remaining cohorts (x-axis) and by 5-shot F1 on the held-out target (y-axis). Diagonal indicates perfect rank preservation. Model rankings transfer reliably across tissue types.

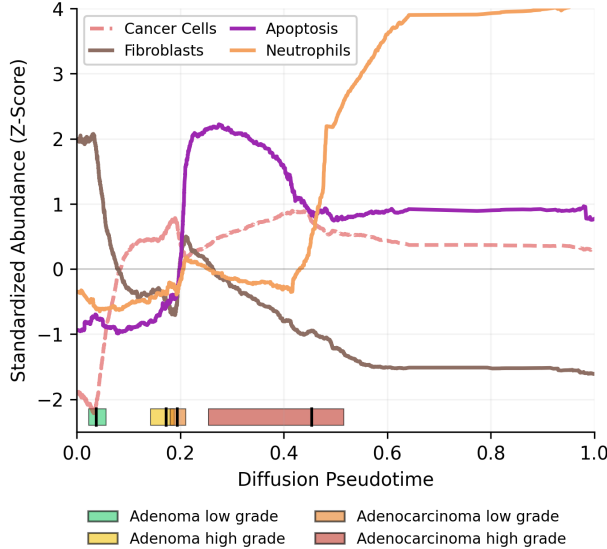


Figure 6. Biological evaluation of the learned trajectory. Biological validation of inferred pseudotime on the colorectal conventional progression cohort. Patch-level cellular composition was quantified using HistoPLUS segmentation; mean proportions are Z-score standardized to compare trends across rare and dominant cell types. Ground-truth class distributions (interquartile range) shown above x-axis (see Appendix Fig. 15).

necessarily whether the representation encodes biological relationships between disease states. In contrast, trajectory fidelity probes a stronger geometric property: not merely that classes are separable, but that their arrangement in representation space reflects the underlying biological process connecting them.

Our biological grounding analysis provides strong support for this distinction. The observed variation in fibroblast and neutrophil abundance across and within disease states aligns with known patterns of stromal remodeling during CRC progression. This level of validation is not accessible through classification metrics, which remain agnostic to inter-class

organization, providing further opportunities to investigate disease progression through DPT-ordered samples.

The geometric constraint imposed by trajectory fidelity also offers a robust signal of generalization. We find that model rankings by reference τ on held-out diseases match rankings by few-shot F1 (mean $\rho = 0.92$), indicating that trajectory fidelity reflects transferable representation quality. Together, these results position τ as a complementary, geometry-based criterion for evaluating representations, offering insight into continuous biological structure while providing a robust proxy for downstream generalization.

5.1. Limitations

Several methodological constraints bound the scope of these findings. Our analysis relies on ergodicity assumptions common to snapshot-based studies: diffusion-based methods can recover relative topological ordering but cannot identify absolute temporal rates. Disease states are defined by coarse ordinal labels; although SPIDER provides patch-level expert annotations with surrounding context, tumor heterogeneity and limited field of view mean patches may lack diagnostic hallmarks of their assigned stage. We evaluated a set of popular CPatch models and a natural image baseline, the observed variations should be interpreted as qualitative trends rather than statistically supported claims about specific design choices. This study focuses on cancer progressions dominated by morphological changes; progressions involving branching trajectories or multiple interacting etiologies may violate the single continuous manifold assumption. Finally, while we leveraged four cohorts from a multi-site, multi-scanner dataset with detailed annotations, it will be important in future work to further assess generalization.

5.2. Conclusion

Our results demonstrate that vision foundation models can represent continuous biological structure beyond what discrete classification benchmarks assess. This opens the door

to progression-level analysis directly in representation space, including understanding disease biology at finer granularity than current classification systems permit. More broadly, the approach may extend to any vision domain where continuous processes are observed through static snapshots, offering a framework to probe whether learned representations capture the dynamics underlying their training data.

Impact Statement

This work is methodological, probing the geometric structure of pathology foundation model representations rather than proposing clinical tools. If such analyses eventually inform clinical interpretation, potential benefits include earlier detection of transition-prone lesions and reduced overtreatment in conditions like DCIS (Hulahan & Angel, 2024). However, pseudotime orderings reflect correlational structure, not causal mechanisms, and the datasets we analyze lack demographic metadata, precluding assessment of performance variation across patient populations.

References

Adjadj, B., Bannier, P.-A., Horent, G., Mandela, S., Lyon, A., Schutte, K., Marteau, U., Gaury, V., Dumont, L., Mathieu, T., consortium, M., Belbahri, R., Schmauch, B., Durand, E., Loga, K. V., and Gillet, L. Towards comprehensive cellular characterisation of h&e slides, 2025. URL <https://arxiv.org/abs/2508.09926>.

Bareja, R., Carrillo-Perez, F., Zheng, Y., Pizurica, M., Nandi, T. N., Shen, J., Madduri, R., and Gevaert, O. Evaluating vision and pathology foundation models for computational pathology: A comprehensive benchmark study. *medRxiv*, 2025. doi: 10.1101/2025.05.08.25327250. URL <https://www.medrxiv.org/content/early/2025/05/12/2025.05.08.25327250>.

Campanella, G., Chen, S., Singh, M., et al. A clinical benchmark of public self-supervised pathology foundation models. *Nature Communications*, 16:3640, 2025. doi: 10.1038/s41467-025-58796-1. URL <https://doi.org/10.1038/s41467-025-58796-1>.

Chen, R. J., Ding, T., Lu, M. Y., Williamson, D. F., Jaume, G., Chen, B., Zhang, A., Shao, D., Song, A. H., Shaban, M., et al. Towards a general-purpose foundation model for computational pathology. *Nature Medicine*, 2024.

de Jong, E. D., Marcus, E., and Teuwen, J. Current pathology foundation models are unrobust to medical center differences, 2025. URL <https://arxiv.org/abs/2501.18055>.

De Palma, F. D. E., D'Argenio, V., Pol, J., Kroemer, G., Maiuri, M. C., and Salvatore, F. The molecular hallmarks of the serrated pathway in colorectal cancer. *Cancers (Basel)*, 11(7):1017, 2019. doi: 10.3390/cancers11071017. URL <https://doi.org/10.3390/cancers11071017>.

Dorszewski, T., Tětková, L., Jenssen, R., Hansen, L. K., and Wickstrøm, K. K. From colors to classes: Emergence of concepts in vision transformers, 2025. URL <https://arxiv.org/abs/2503.24071>.

Facco, E., d'Errico, M., Rodriguez, A., and Laio, A. Estimating the intrinsic dimension of datasets by a minimal neighborhood information. *Scientific Reports*, 7(1):12140, 2017. doi: 10.1038/s41598-017-11873-y. URL <https://doi.org/10.1038/s41598-017-11873-y>.

Fearon, E. R. and Vogelstein, B. A genetic model for colorectal tumorigenesis. *Cell*, 61(5):759–767, 1990. doi: 10.1016/0092-8674(90)90186-I. URL [https://doi.org/10.1016/0092-8674\(90\)90186-I](https://doi.org/10.1016/0092-8674(90)90186-I).

Fleming, M., Ravula, S., Tatishchev, S. F., and Wang, H. L. Colorectal carcinoma: Pathologic aspects. *Journal of Gastrointestinal Oncology*, 3(3):153–173, 2012. doi: 10.3978/j.issn.2078-6891.2012.030.

Haghverdi, L., Büttner, M., Wolf, F. A., Buettner, F., and Theis, F. J. Diffusion pseudotime robustly reconstructs lineage branching. *Nature Methods*, 13(10):845–848, 2016. doi: 10.1038/nmeth.3971. URL <https://doi.org/10.1038/nmeth.3971>.

Hulahan, T. S. and Angel, P. M. From ductal carcinoma in situ to invasive breast cancer: the prognostic value of the extracellular microenvironment. *Journal of Experimental & Clinical Cancer Research*, 43(1):329, 2024. doi: 10.1186/s13046-024-03236-z. URL <https://jeccr.biomedcentral.com/articles/10.1186/s13046-024-03236-z>.

Kalluri, R. The biology and function of fibroblasts in cancer. *Nature Reviews Cancer*, 16(9):582–598, 2016. doi: 10.1038/nrc.2016.73.

Kang, M., Song, H., Park, S., Yoo, D., and Pereira, S. Benchmarking self-supervised learning on diverse pathology datasets, 2023. URL <https://arxiv.org/abs/2212.04690>.

Kendall, M. G. A new measure of rank correlation. *Biometrika*, 30(1-2):81–93, 1938. doi: 10.1093/biomet/30.1-2.81. URL <https://doi.org/10.1093/biomet/30.1-2.81>.

Kömen, J., Marienwald, H., Dippel, J., and Hense, J. Do histopathological foundation models eliminate batch effects? a comparative study. In *Advancements In Medical*

Foundation Models: Explainability, Robustness, Security, and Beyond, 2024. URL <https://openreview.net/forum?id=Ty0Z1JOZQ0>.

Lu, M. Y., Chen, B., Williamson, D. F., Chen, R. J., Liang, I., Ding, T., Jaume, G., Odintsov, I., Le, L. P., Gerber, G., et al. A visual-language foundation model for computational pathology. *Nature Medicine*, 30:863–874, 2024.

Nechaev, D., Pchelnikov, A., and Ivanova, E. Histai: An open-source, large-scale whole slide image dataset for computational pathology, 2025a. URL <https://arxiv.org/abs/2505.12120>.

Nechaev, D., Pchelnikov, A., and Ivanova, E. Spider: A comprehensive multi-organ supervised pathology dataset and baseline models, 2025b. URL <https://arxiv.org/abs/2503.02876>.

Oquab, M., Darzet, T., Moutakanni, T., Vo, H., Szafraniec, M., Khalidov, V., Fernandez, P., Haziza, D., Massa, F., El-Nouby, A., Assran, M., Ballas, N., Galuba, W., Howes, R., Huang, P.-Y., Li, S.-W., Misra, I., Rabbat, M., Sharma, V., Synnaeve, G., Xu, H., Jegou, H., Mairal, J., Labatut, P., Joulin, A., and Bojanowski, P. Dinov2: Learning robust visual features without supervision, 2024. URL <https://arxiv.org/abs/2304.07193>.

Raghu, M., Unterthiner, T., Kornblith, S., Zhang, C., and Dosovitskiy, A. Do vision transformers see like convolutional neural networks?, 2022. URL <https://arxiv.org/abs/2108.08810>.

Ratushny, V., Gober, M. D., Hick, R., Ridky, T. W., and Seykora, J. T. From keratinocyte to cancer: the pathogenesis and modeling of cutaneous squamous cell carcinoma. *Journal of Clinical Investigation*, 122(2):464–472, February 2012. doi: 10.1172/JCI57415. URL <https://doi.org/10.1172/JCI57415>.

Schlemper, R. J., Riddell, R. H., Kato, Y., Borchard, F., Cooper, H. S., Dawsey, S. M., Dixon, M. F., Fenoglio-Preiser, C. M., Fléjou, J. F., Geboes, K., Hattori, T., Hirata, T., Itabashi, M., Iwafuchi, M., Iwashita, A., Kim, Y. I., Kirchner, T., Klmpfinger, M., Koike, M., Lauwers, G. Y., Lewin, K. J., Oberhuber, G., Offner, F., Price, A. B., Rubio, C. A., Shimizu, M., Shimoda, T., Sipponen, P., Solcia, E., Stolte, M., Watanabe, H., and Yamabe, H. The Vienna classification of gastrointestinal epithelial neoplasia. *Gut*, 47(2):251–255, 2000. doi: 10.1136/gut.47.2.251.

Shaul, M. E. and Fridlander, Z. G. Tumour-associated neutrophils in patients with cancer. *Nature Reviews Clinical Oncology*, 16(10):601–620, 2019. ISSN 1759-4782. doi: 10.1038/s41571-019-0222-4. URL <https://doi.org/10.1038/s41571-019-0222-4>.

Tizhoosh, H. R. Beyond the failures: Rethinking foundation models in pathology, 2025. URL <https://arxiv.org/abs/2510.23807>.

Ueno, H., Kajiwara, Y., Ajioka, Y., Sugai, T., Sekine, S., Ishiguro, M., Takashima, A., and Kanemitsu, Y. Histopathological atlas of desmoplastic reaction characterization in colorectal cancer. *Japanese Journal of Clinical Oncology*, 51(6):1004–1012, 2021. doi: 10.1093/jjco/hyab040.

Wang, W., Bao, H., Dong, L., Bjorck, J., Peng, Z., Liu, Q., Aggarwal, K., Mohammed, O. K., Singhal, S., Som, S., and Wei, F. Image as a foreign language: Beit pretraining for all vision and vision-language tasks, 2022. URL <https://arxiv.org/abs/2208.10442>.

Wolf, F. A., Angerer, P., and Theis, F. J. SCANPY: large-scale single-cell gene expression data analysis. *Genome Biology*, 19(15), 2018. doi: 10.1186/s13059-017-1382-0. URL <https://doi.org/10.1186/s13059-017-1382-0>.

Xiang, J., Wang, X., Zhang, X., Xi, Y., Eweje, F., Chen, Y., Li, Y., Bergstrom, C., Gopaulchan, M., Kim, T., Yu, K.-H., Willens, S., Olguin, F. M., Nirschl, J. J., Neal, J., Diehn, M., Yang, S., and Li, R. A vision-language foundation model for precision oncology. *Nature*, 638:769–778, 2025. doi: 10.1038/s41586-024-08378-w. URL <https://doi.org/10.1038/s41586-024-08378-w>.

Xu, H., Usuyama, N., Bagga, J., Zhang, S., Rao, R., Naumann, T., Wong, C., Gero, Z., González, J., Gu, Y., Xu, Y., Wei, M., Wang, W., Ma, S., Wei, F., Yang, J., Li, C., Gao, J., Rosemon, J., Bower, T., Lee, S., Weerasinghe, R., Wright, B. J., Robicsek, A., Piening, B., Bifulco, C., Wang, S., and Poon, H. A whole-slide foundation model for digital pathology from real-world data. *Nature*, 2024.

Zeiler, M. D. and Fergus, R. Visualizing and understanding convolutional networks. In Fleet, D., Pajdla, T., Schiele, B., and Tuytelaars, T. (eds.), *Computer Vision – ECCV 2014*, volume 8689 of *Lecture Notes in Computer Science*, pp. 818–833, Cham, 2014. Springer. doi: 10.1007/978-3-319-10590-1_53. URL https://link.springer.com/chapter/10.1007/978-3-319-10590-1_53.

Zimmermann, E., Vorontsov, E., Viret, J., Casson, A., Zelechowski, M., Shaikovski, G., Tenenholz, N., Hall, J., Klimstra, D., Yousfi, R., Fuchs, T., Fusi, N., Liu, S., and Severson, K. Virchow2: Scaling self-supervised mixed magnification models in pathology, 2024. URL <https://arxiv.org/abs/2408.00738>.

A. DPT Hyperparameter Selection

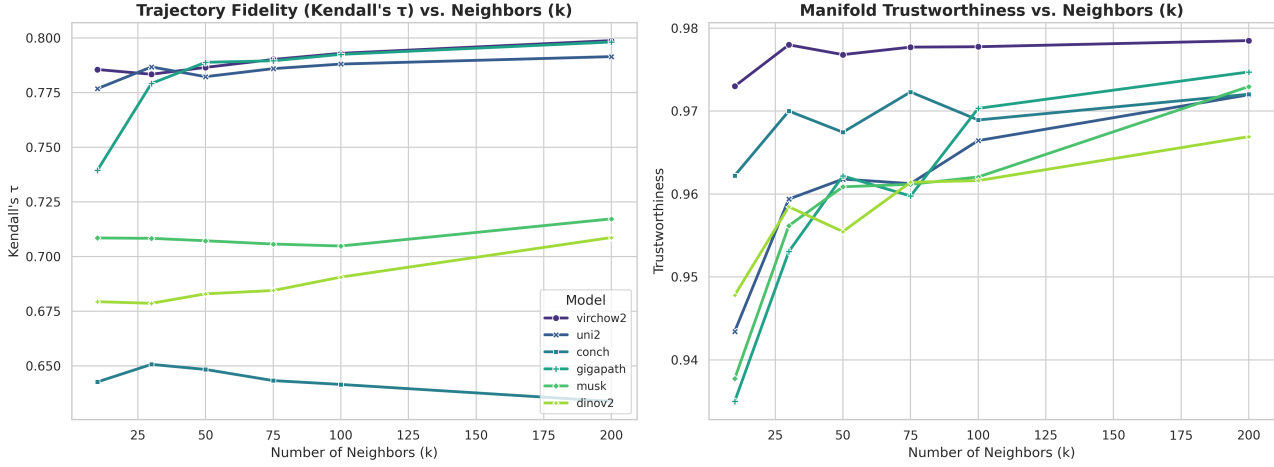


Figure 7. Sensitivity analysis of the neighborhood parameter k . We evaluated the impact of the number of nearest neighbors (k) on trajectory fidelity (Kendall's τ) and manifold trustworthiness using the CRC-Serrated cohort. Trajectory fidelity (left) exhibits a stable plateau for $k \geq 50$ across leading pathology models, while trustworthiness (right) suggests that $k = 100$ effectively preserves the local structure of the high-dimensional embeddings during diffusion mapping.

To apply the diffusion pseudotime method, the algorithm requires setting several hyperparameters:

- **Root Selection.** Diffusion pseudotime requires designating a root sample as time zero. We use the medoid of the earliest disease class, which approximates the biological starting point without requiring manual selection. Sensitivity to root choice is limited: even if the selected root happens to represent an advanced case within the earliest class, a well-organized embedding space will still recover the correct global ordering, though early-stage samples may exhibit increased pseudotime variance.
- **Density Norm (α):** We set $\alpha = 0$ as it yielded superior spectral stability and trajectory fidelity across all cohorts. This choice is consistent with our balanced sampling strategy ($N = 1,000$ per class), which ensures approximately uniform density across progression stages. We observed that $\alpha = 1$ (Laplace-Beltrami normalization) resulted in degraded performance, likely due to the inherent difficulty of accurate density estimation in high-dimensional embedding spaces and a heightened sensitivity to local manifold outliers. Our final configuration is empirically validated by high manifold trustworthiness scores (> 0.97) and stable eigengaps (see Appendix D).
- **Diffusion Components:** We fixed the number of diffusion components at $n_{dc} = 10$ for all experiments. This choice was informed by our intrinsic dimension (ID) analysis (Section 4.2), which estimated the manifold dimensionality to be ≈ 4.5 across all pathology-specific models. We chose a component count that exceeds the estimated ID by a factor of two to ensure complete capture of the biological progression signal while simultaneously acting as a spectral low-pass filter to exclude high-frequency noise and technical artifacts.
- **K Nearest Neighbors:** We selected $k = 100$ as the primary neighborhood size based on a hyperparameter sweep ($k \in [10, 200]$) evaluating Trajectory Fidelity and Manifold Trustworthiness. As shown in Figure 7, trajectory fidelity remains stable for $k \geq 50$ across all high-performing pathology models. While Trustworthiness continues to show marginal gains up to $k = 200$, the $k = 100$ threshold represents a point of diminishing returns where the manifold structure is sufficiently captured without incurring the quadratic computational cost associated with larger neighborhood graph construction and multiscale diffusion distance calculations.

DPT Limitations. DPT assumes a connected branching structure and cannot model cyclic processes or disconnected subpopulations. The method requires specifying a root, which we set using prior biological knowledge; alternative root choices could yield different orderings. Successful pseudotime recovery demonstrates that the embedding geometry aligns with progression, but does not reveal which specific features drive this alignment or whether the model has learned causal

mechanisms versus correlates. We interpret our results as evidence of progression-relevant structure, not mechanistic understanding.

B. Slide Aware Sampling

To ensure trajectory fidelity reflects generalizable model properties rather than slide-level batch effects, we implemented slide-aware sampling that controls for hierarchical structure in histopathology data. Naive random sampling would oversample densely-tiled WSIs while undersampling sparse ones, confounding trajectory inference with intra-slide correlations.

B.1. Sampling Procedure

For each disease progression cohort, we sample n patches per class while enforcing a maximum of m patches per slide:

For each class in the progression, we group patches by their source slide and shuffle the slide order. We then iterate through slides, taking up to $m_{\text{max_per_slide}}$ patches from each (shuffled within-slide) until reaching $n_{\text{per_class}}$ total patches for that class. This ensures patches are drawn from diverse slides rather than concentrated in densely-tiled WSIs. All models are evaluated on identical patch sets, established via a reference model’s registry and validated at load time.

B.2. Bootstrap Resampling

For confidence interval estimation, we employ stratified bootstrap resampling: patches are partitioned by ground-truth class, then resampled with replacement within each class while maintaining original class-wise sample sizes.

B.3. Implementation Parameters

Bootstrap iterations of 100 was picked to balance robustness with the high computational cost of recomputing the analysis.

The choice of $m = 50$ balances within-slide morphological coverage against preventing any single slide from dominating trajectory inference. Combined with diffusion pseudotime’s k -nearest-neighbor graph ($k = 100$), this reduces the likelihood that neighbor relationships are dominated by patches sharing preparation artifacts or scanner characteristics.

The number of patches per class was set to 1000 due to dataset size, and the desire to sample from multiple slides.

C. Trajectory Fidelities for all models and progressions

In Table 1, we show all trajectory fidelities for all disease progressions and models, with the 95% confidence intervals.

D. Manifold Robustness and Methodological Justification

To verify that our manifold inference is robust to local variations in sampling density—particularly for the BDC cohort ($N = 2,714$)—we evaluated the topological stability and dimensionality of the recovered representations.

Table 1. Trajectory fidelity (τ) scores across models and disease progressions. Values shown with 95% confidence intervals.

Model	Progression	τ	95% CI
DINOv2	BDC	0.22	[0.01, 0.28]
	CRC-Conventional	0.52	[0.40, 0.59]
	CRC-Serrated	0.69	[0.47, 0.71]
	SCC	0.48	[0.12, 0.50]
CONCH	BDC	0.60	[0.53, 0.65]
	CRC-Conventional	0.70	[0.52, 0.73]
	CRC-Serrated	0.64	[0.62, 0.69]
	SCC	0.64	[0.57, 0.66]
MuSK	BDC	0.34	[0.29, 0.54]
	CRC-Conventional	0.68	[0.56, 0.71]
	CRC-Serrated	0.70	[0.51, 0.71]
	SCC	0.64	[0.44, 0.67]
UNI-2	BDC	0.70	[0.65, 0.72]
	CRC-Conventional	0.72	[0.57, 0.74]
	CRC-Serrated	0.79	[0.77, 0.79]
	SCC	0.71	[0.49, 0.72]
Virchow-2	BDC	0.62	[0.56, 0.66]
	CRC-Conventional	0.73	[0.72, 0.74]
	CRC-Serrated	0.79	[0.79, 0.80]
	SCC	0.72	[0.70, 0.73]
Prov-GigaPath	BDC	0.54	[0.45, 0.61]
	CRC-Conventional	0.74	[0.66, 0.75]
	CRC-Serrated	0.79	[0.75, 0.80]
	SCC	0.59	[0.57, 0.62]

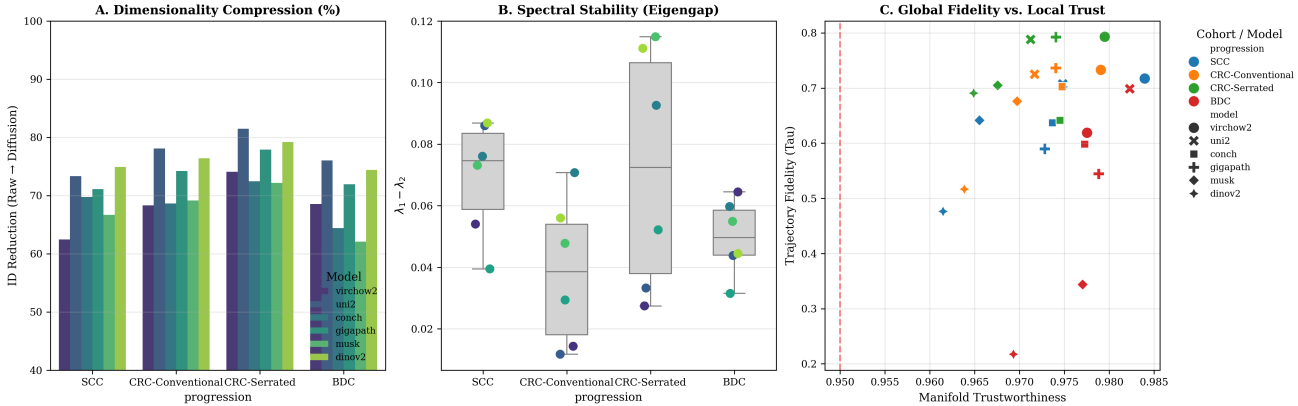


Figure 8. Manifold Stability and Denoising Proof. (A) Dimensionality compression shows the percentage reduction from raw embedding ID to diffusion manifold ID. Values $> 60\%$ across all cohorts indicate successful denoising. (B) The spectral gap ($\lambda_1 - \lambda_2$) remains stable across all progressions; notably, the BDC cohort exhibits connectivity comparable to larger cohorts, justifying our slide-aware sampling strategy. (C) Global trajectory fidelity (τ) is plotted against local manifold trustworthiness. High trustworthiness (> 0.95) across all models ensures that the pseudotime trajectory is grounded in local morphological similarity without significant topological distortion.

D.1. Intrinsic Dimension and Topological Denoising

A core justification for using Diffusion Pseudotime (DPT) is its ability to perform topological denoising. As shown in Figure 8A, we observe a consistent reduction in intrinsic dimensionality (ID) of approximately 70% across all models and cohorts.

For example, in the Virchow-2 BDC manifold, the ID is reduced from 12.7 to 4.0. This significant compression indicates that the diffusion operator successfully identifies a low-dimensional biological manifold from within the high-dimensional, noisy embedding space.

D.2. Empirical Validation of the BDC Cohort

Readers may note that the BDC cohort contains fewer patches ($N = 2,714$) than other cohorts ($N = 4,000$). However, our analysis suggests that the *diversity* of the support is more critical than raw density. The BDC cohort exhibits a mean spectral gap of 0.050, which is higher than that of the CRC-Conventional cohort (0.038), despite the latter having 47% more samples. Furthermore, BDC achieved the highest mean manifold trustworthiness (0.977) among all progressions. These results prove that our slide-aware sampling (max 50 patches per slide) preserved the connectivity required for stable manifold inference even in data-constrained scenarios.

Table 2. Aggregated Manifold Quality Metrics. Mean values calculated across all six foundation models. BDC metrics demonstrate mathematical parity with larger cohorts.

Progression	Spectral Gap	ID Reduction (%)	Trustworthiness	Avg. τ
BDC	0.050	69.57%	0.977	0.504
CRC-Conventional	0.038	72.47%	0.972	0.682
CRC-Serrated	0.072	76.20%	0.972	0.735
SCC	0.069	69.70%	0.972	0.628

E. Permutation Test Details

Figure 9 presents the permutation test results stratified by disease progression. While the averaged results (Figure 3) demonstrate that all models encode progression structure beyond class separation, the per-progression view reveals cohort-specific variation. BDC proved most challenging: DINOv2 and MuSK yielded τ values within or near the null distribution, suggesting these models fail to capture the continuous morphological changes in breast ductal carcinoma progression. In contrast, vision-only pathology models maintained clear separation from null across all four progressions, indicating more robust encoding of biological continuity.

F. Absolute Depth Analysis

We analyzed trajectory fidelity emergence across three token types: patch mean, CLS, and register mean. Figure 10–12 present three-panel analyses for each, showing trajectory fidelity versus relative depth, intrinsic dimensionality divergence, and trajectory fidelity versus absolute transformer block index.

G. Trajectory Fidelity and Classification Performance

This appendix provides methodological details for the analyses in Section 4.3, which examine the relationship between trajectory fidelity (τ) and few-shot classification performance.

G.1. Within-Disease Correlation

We first assessed whether trajectory fidelity correlates with classification performance when both metrics are measured on the same disease progression.

Few-Shot Classification. We trained logistic regression probes with limited labeled examples to evaluate discriminative performance. For each trial, we sampled exactly $k = 5$ patches per class uniformly at random (without replacement) for training, reserving all remaining patches for evaluation. Embeddings were z-score normalized using statistics computed solely from the training samples. We report macro-averaged F1 scores to account for class imbalance. To reduce sampling variance, we repeated each experiment across $N = 10$ random trials and report mean performance.

Correlation Analysis. For each of the four disease progressions independently, we computed two metrics for each model:

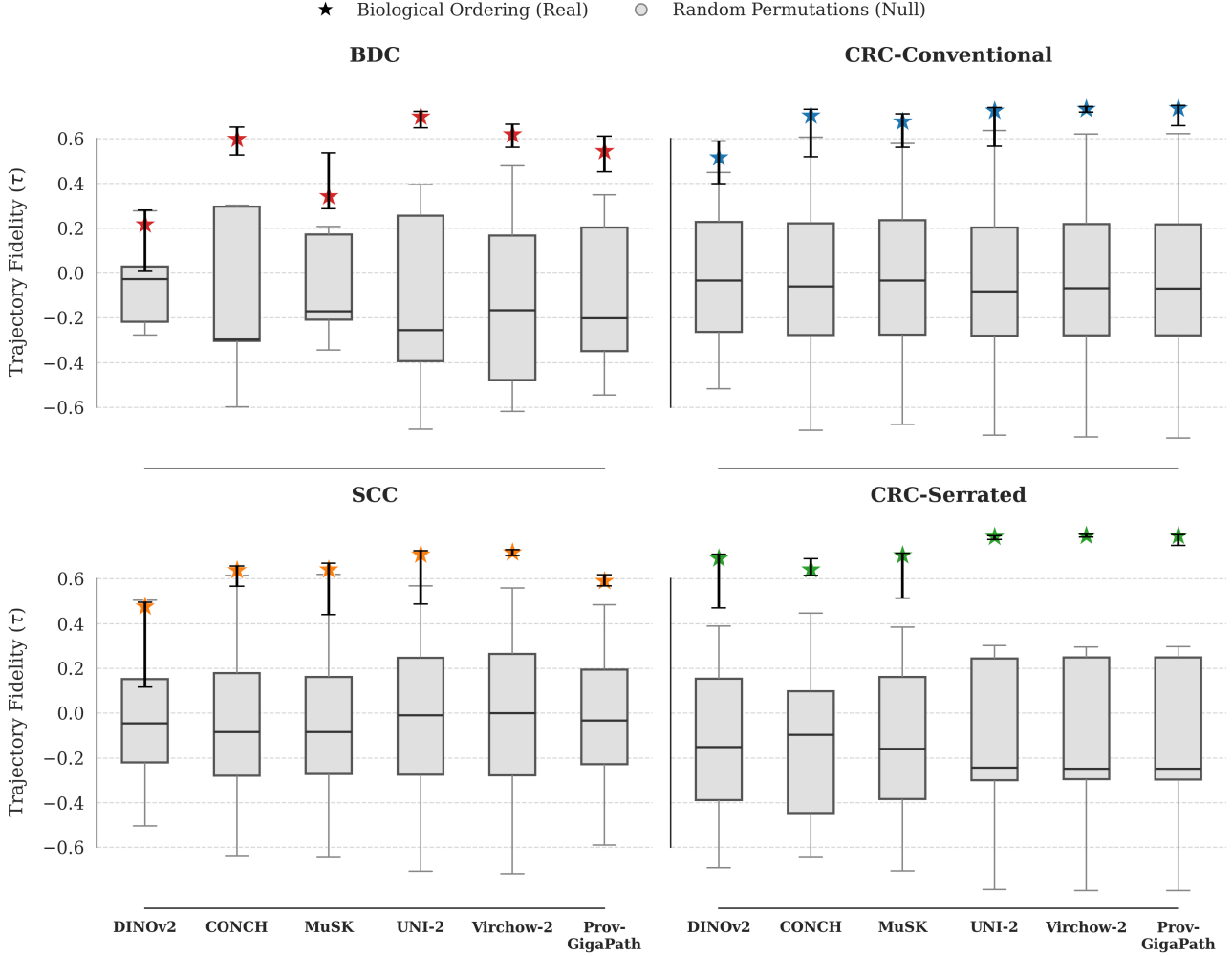


Figure 9. Per-progression permutation test results. Stars indicate τ for the true biological ordering (with 95% CI); boxplots show null distributions from all possible class order permutations. BDC exhibited the most model-dependent variation: DINOv2 and MuSK approached null performance while vision-only pathology models (UNI-2, Virchow-2, Prov-GigaPath) maintained strong separation. Colorectal progressions (CRC-Conventional, CRC-Serrated) and SCC showed consistent separation from null across all models.

1. **Trajectory fidelity (τ):** Kendall’s τ between diffusion pseudotime and ordinal stage labels, calculated from final-layer embeddings as described in Section 3.
2. **5-shot F1:** Mean macro-averaged F1 score from the few-shot classification protocol above.

We then computed Spearman’s rank correlation (ρ) between these two metrics across the six models, yielding one correlation coefficient per disease progression.

Results. Figure 13 shows consistently strong correlations: $\rho = 0.94$ (BDC), $\rho = 0.83$ (SCC), $\rho = 0.77$ (CRC-Conv), and $\rho = 0.77$ (CRC-Serr), with a mean of $\rho = 0.83$. This indicates that, controlling for disease-specific baseline difficulty, models that better preserve progression geometry achieve substantially higher few-shot classification performance.

G.2. Cross-Task Generalization

We next tested whether trajectory fidelity on reference diseases predicts few-shot classification performance on held-out diseases, providing evidence that τ captures transferable aspects of representation quality rather than disease-specific structure.

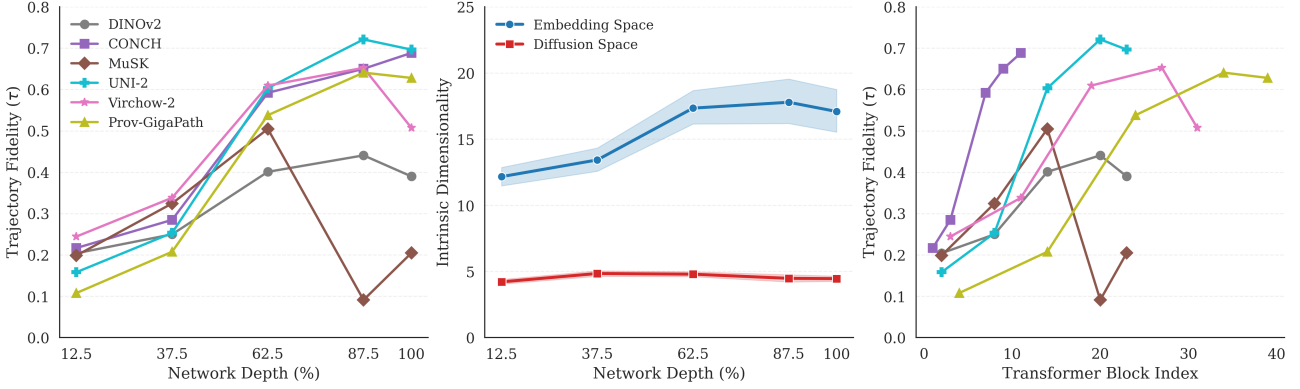


Figure 10. Emergence analysis: Patch mean embeddings. *Left:* Trajectory fidelity (τ) versus relative network depth. Steepest gains occur between 30–60% depth; vision-only models continue improving through 87.5%. MuSK collapses after 62.5%. *Center:* Raw embedding intrinsic dimensionality (blue) expands while diffusion manifold dimensionality (red, ≈ 4.5) remains stable. *Right:* Absolute block index obscures the consistent relative-depth pattern due to varying model sizes (12–40 blocks).

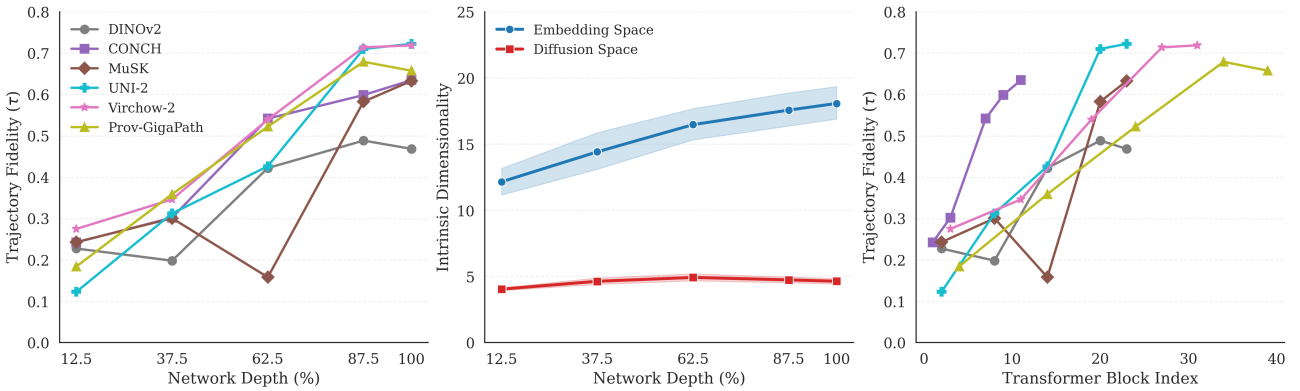


Figure 11. Emergence analysis: CLS token embeddings. *Left:* CLS tokens show more monotonic trajectory fidelity increase compared to patch mean, particularly for vision-only models (UNI-2, Virchow-2, Prov-GigaPath) which improve steadily through final layers. MuSK exhibits the same mid-depth collapse as in patch mean, though less severe (recovering partially by 100%). *Center:* Intrinsic dimensionality patterns mirror those of patch mean. *Right:* Absolute depth view.

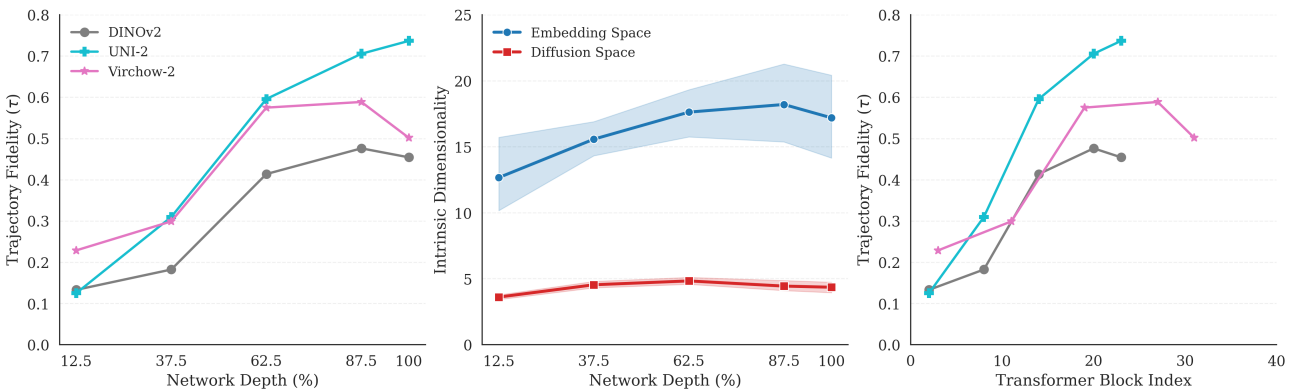


Figure 12. Emergence analysis: Register mean embeddings. Only models with register tokens are shown (DINOv2, UNI-2, Virchow-2). *Left:* Register tokens show the steepest and most consistent emergence curves, with UNI-2 achieving the highest trajectory fidelity ($\tau > 0.7$). Virchow-2 shows a slight decline after 87.5% depth. *Center:* Intrinsic dimensionality patterns are consistent with other token types, though with wider confidence intervals due to fewer models. *Right:* Absolute depth view confirms the relative-depth normalization aligns emergence across architectures.

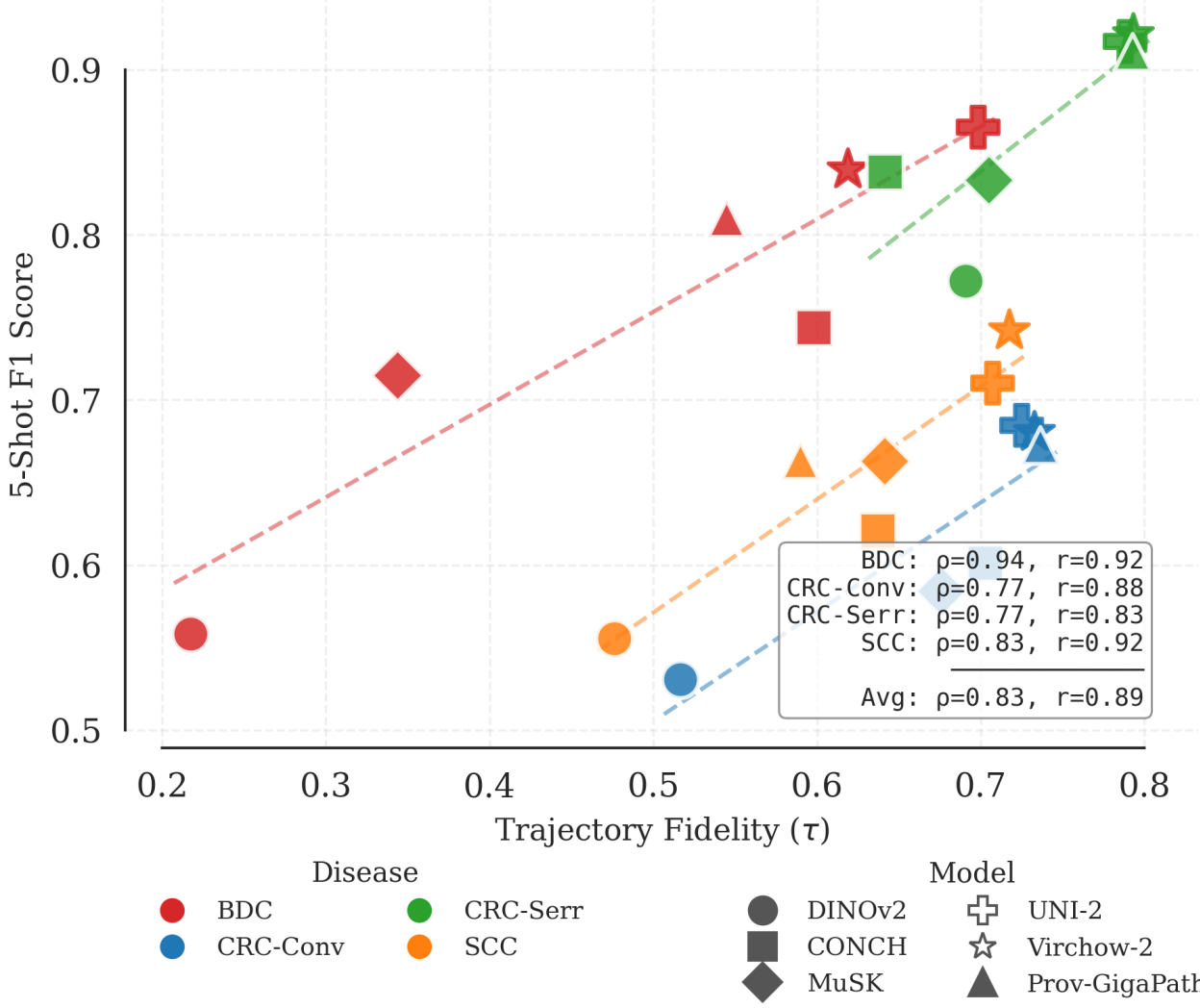


Figure 13. Trajectory fidelity correlates with classification performance within each disease. For each progression (panel), we plot trajectory fidelity (τ , x-axis) against 5-shot classification F1 (y-axis) for each model. Correlations are consistently strong across all four diseases (mean $\rho = 0.83$), indicating that models preserving progression structure also achieve better discriminative performance.

Leave-One-Out Protocol. We employed a leave-one-out cross-validation design across the four disease progressions. For each iteration:

1. **Designate target:** One progression was held out as the target task.
2. **Compute reference τ :** For each model, we calculated the mean trajectory fidelity across the three remaining (reference) progressions.
3. **Evaluate held-out F1:** We measured 5-shot classification F1 on the held-out target progression using the same few-shot protocol described above.
4. **Correlate:** We computed Spearman’s ρ between reference τ and held-out F1 across the six models.

This yields four correlation coefficients (one per target task), which we summarize by their mean.

Results. Figure 5 (main text) shows that reference trajectory fidelity strongly predicts held-out classification performance: $\rho = 1.00$ (CRC-Conv), $\rho = 0.94$ (BDC), $\rho = 0.89$ (SCC), and $\rho = 0.83$ (CRC-Serr), with a mean of $\rho = 0.92$. This indicates that model rankings by trajectory fidelity on reference diseases reliably transfer to held-out tissue types.

Comparison with Classification as Reference Metric. To assess whether trajectory fidelity offers unique predictive value, we compared it against classification performance as an alternative reference metric. Using the same leave-one-out protocol, we computed both reference τ (mean trajectory fidelity on three cohorts) and reference F1 (mean 5-shot classification F1 on three cohorts) for each model, then correlated each with held-out F1 on the fourth cohort.

Figure 14 shows that both metrics predict held-out performance with comparable accuracy: reference τ achieves mean $\rho = 0.91$ across target tasks, while reference F1 achieves mean $\rho = 0.91$. This equivalence suggests that trajectory fidelity and classification performance both capture aspects of representation quality that generalize across tissue types. The practical value of τ lies not in superior prediction, but in its biological interpretability: trajectory fidelity directly quantifies whether models encode disease as a continuous process, providing mechanistic insight that classification accuracy alone cannot offer.

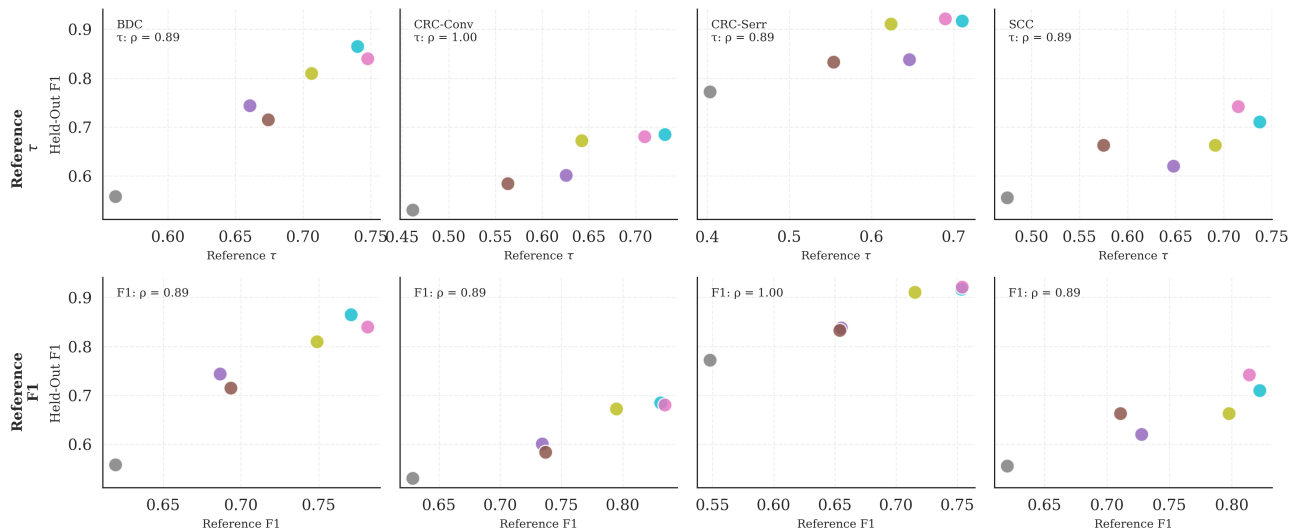


Figure 14. Trajectory fidelity and classification performance are equivalent predictors of cross-task generalization. We compared reference τ (top row) and reference F1 (bottom row) as predictors of held-out 5-shot classification performance using a leave-one-out protocol across four disease progressions. Each column represents a different held-out target task. Both metrics achieve comparable predictive accuracy (mean $\rho = 0.91$), indicating they capture complementary aspects of transferable representation quality. Points represent individual foundation models; lines show linear fits for visualization.

H. Pseudotime HistoPLUS Analysis: Sampling Diagnostics

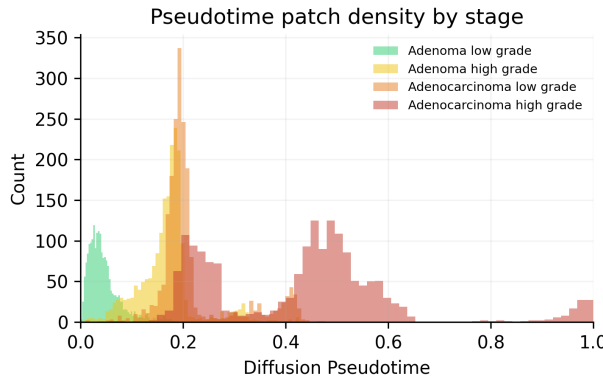
To verify that the biological trends observed along pseudotime are well supported by the underlying patch distribution and are not artifacts of smoothing, we report pseudotime density, local sampling support, and robustness of smoothed trajectories to the smoothing window fraction. This analysis is available in Figure 15

H.1. Cell Type Composition Along Pseudotime

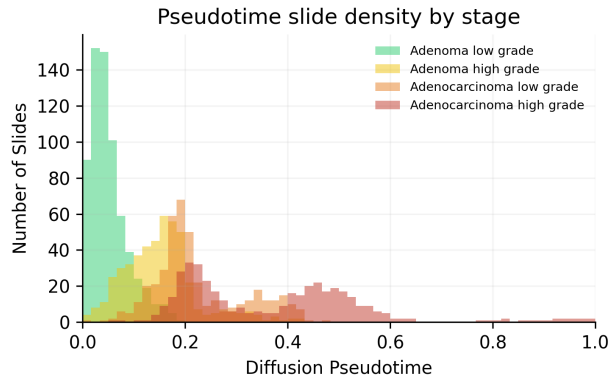
To provide comprehensive detail on cellular changes along the pseudotime trajectory, we present the full cell type composition analysis in Figure 16. This figure complements the main text by showing all 13 cell types identified by HistoPLUS, rather than the subset highlighted in the primary analysis.

H.2. Pseudotime: Additional Sampled Trajectory

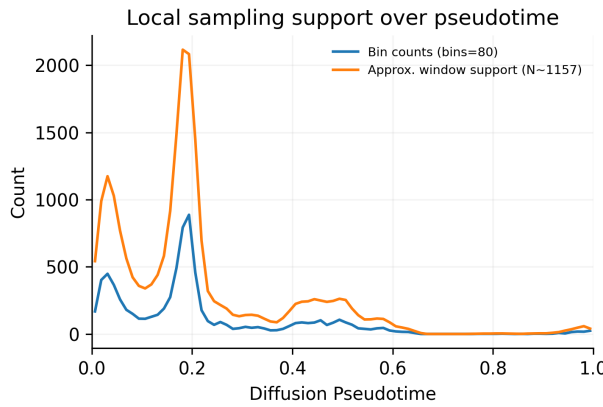
As visualized in Figure 17, by establishing a pseudotime trajectory, we can systematically sample patches along the continuum of disease progression. This capability moves beyond simple classification and allows for the reconstruction of a “morphological movie” from non-temporal data.



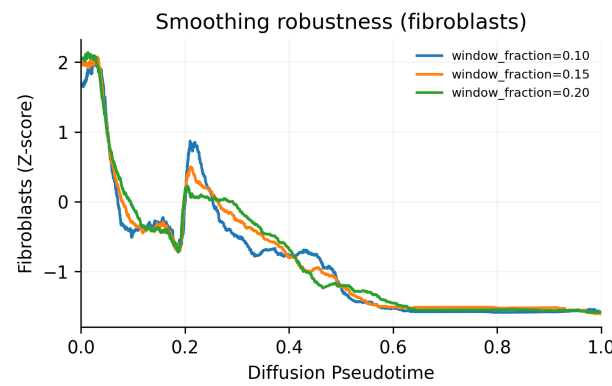
(a) Density by class. Adjacent classes exhibit substantial overlap, indicating that pseudotime captures within-class heterogeneity rather than discrete label separation.



(b) Density by slides. Patches are sampled from slides. We plot slide density by pseudotime to show that a variety of slides contribute patches across the pseudotime continuum.



(c) Local sampling support. Bin counts and estimated rolling-window support confirm that key transition regions are supported by substantial data.



(d) Smoothing robustness. The non-monotonic fibroblast trajectory persists across smoothing window fractions (0.10–0.20).

Figure 15. Pseudotime sampling and robustness diagnostics. Class-wise density demonstrate strong sampling support along the trajectory, where pseudotime < 0.6 , where we focus our analysis. Local support and smoothing analyses confirm that observed cell-type trends are stable and not artifacts of uneven sampling or smoothing choices.

This approach holds significant theoretical utility for computational pathology:

- **Hypothesis Generation for Transitional States:** By observing patches in the pseudotime ranges where classifications have boundaries or overlap, researchers can identify specific morphological features that precede distinct clinical endpoints. This could be used to generate testable hypotheses regarding early markers of progression in CRC and other progressive diseases.
- **Grounding Latent Representations:** Abstract low-dimensional embeddings can be difficult to interpret biologically. Connecting specific trajectory coordinates directly back to representative histology patches provides necessary biological grounding, validating that the model is tracking relevant morphological changes rather than technical artifacts.
- **Refining Pathological Spectra:** This visualization tool can help redefine grading systems to allow for more continuous grading by providing quantitative analysis of progression features.

While these trajectories represent modeled morphological evolution rather than literal temporal data, they provide a powerful, grounded framework for exploring the mechanisms of disease progression in an unprecedented way.

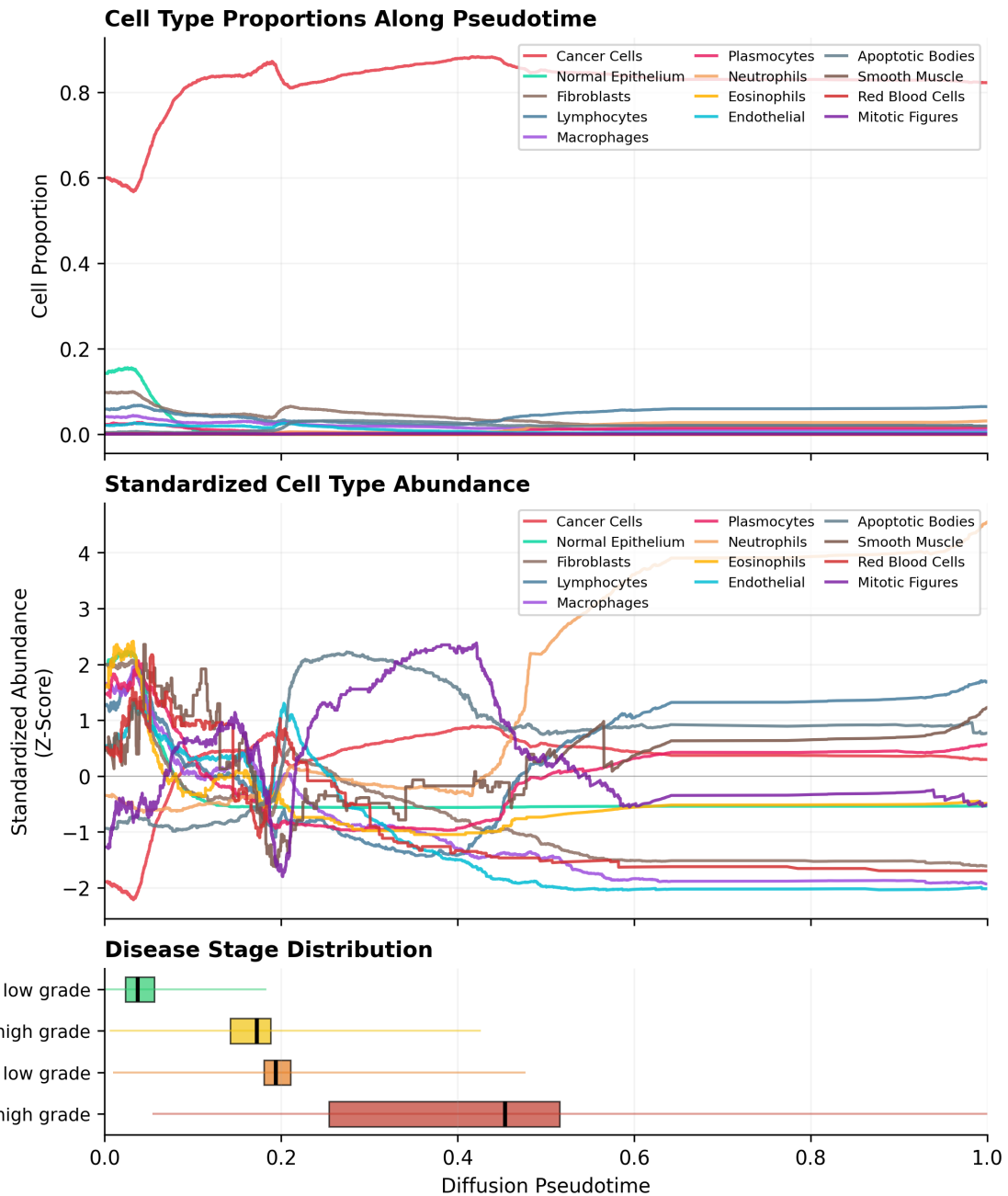


Figure 16. Complete cell type composition along pseudotime. **Top:** Raw cell proportions (smoothed) for all 13 cell types across the pseudotime trajectory. **Middle:** Z-score standardized abundance enables comparison of trends across cell types with different baseline frequencies, revealing coordinated changes in low-abundance populations that would otherwise be obscured. **Bottom:** Disease stage distribution along pseudotime, showing interquartile ranges (boxes), medians (vertical lines), and full ranges (whiskers) for each diagnostic category. Stage overlap along pseudotime reflects the continuous nature of morphological progression captured by the model.

H.3. Reproducibility

The code to produce this analysis is available at https://github.com/pritika-vig/embeddings_disease_progression_analysis.

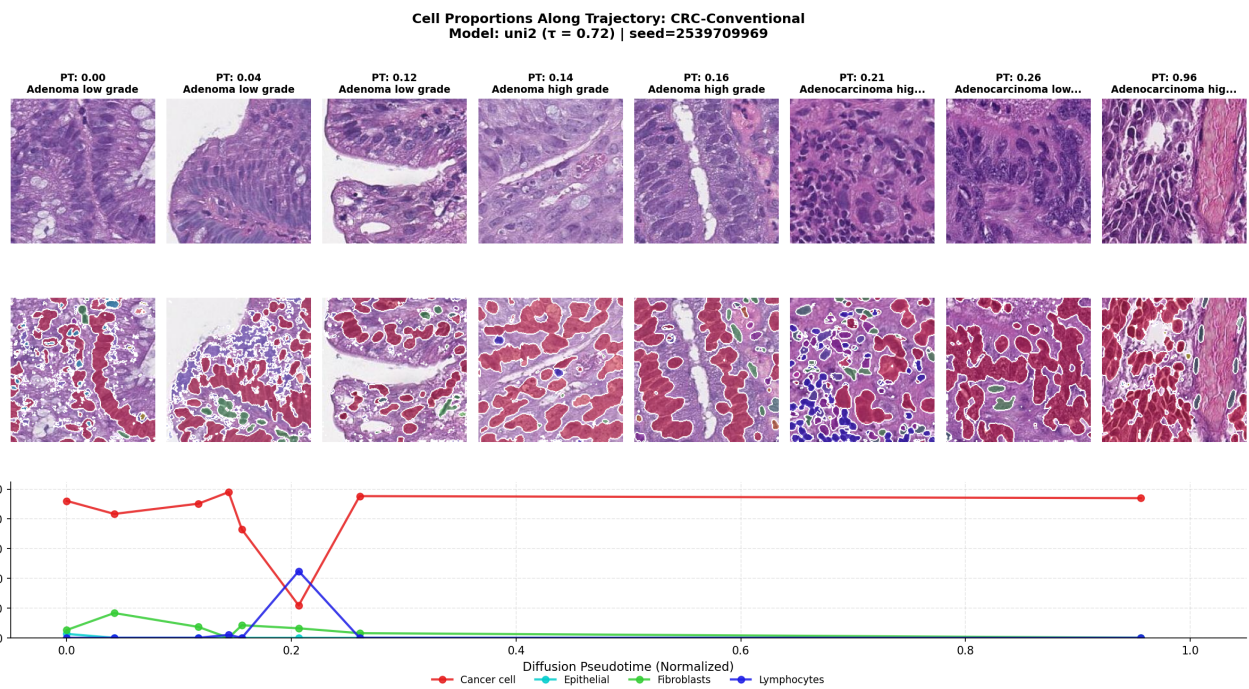


Figure 17. Visualizing morphological disease progression via pseudotime sampling. The top row shows representative patches sampled at increasing pseudotime points along that trajectory. The second row shows the same images, with cell segmentation masks from HistoPLUS. The bottom row shows cell proportion patterns across the sampled patches. This visualization highlights the progressive morphological changes from relatively ordered tissue structures to increasingly disorganized and malignant phenotypes in CRC, captured by the model’s pseudotime progression.